



Title	Meandering Subtropical Jet and Precipitation over Summertime East Asia and the Northwestern Pacific
Author(s)	Horinouchi, Takeshi; Hayashi, Ayumu
Citation	Journal of the Atmospheric Sciences, 74(4), 1233-1247 https://doi.org/10.1175/JAS-D-16-0252.1
Issue Date	2017-04
Doc URL	http://hdl.handle.net/2115/67243
Rights	© Copyright 2017 American Meteorological Society (AMS). Permission to use figures, tables, and brief excerpts from this work in scientific and educational works is hereby granted provided that the source is acknowledged. Any use of material in this work that is determined to be "fair use" under Section 107 of the U.S. Copyright Act September 2010 Page 2 or that satisfies the conditions specified in Section 108 of the U.S. Copyright Act (17 USC § 108, as revised by P.L. 94-553) does not require the AMS' s permission. Republication, systematic reproduction, posting in electronic form, such as on a website or in a searchable database, or other uses of this material, except as exempted by the above statement, requires written permission or a license from the AMS. All AMS journals and monograph publications are registered with the Copyright Clearance Center (http://www.copyright.com). Questions about permission to use materials for which AMS holds the copyright can also be directed to the AMS Permissions Officer at permissions@ametsoc.org . Additional details are provided in the AMS Copyright Policy statement, available on the AMS website (http://www.ametsoc.org/CopyrightInformation).
Type	article
File Information	jas-d-16-0252.1.pdf



[Instructions for use](#)

Meandering Subtropical Jet and Precipitation over Summertime East Asia and the Northwestern Pacific

TAKESHI HORINOUCHI

Faculty of Environmental Earth Science, Hokkaido University, Hokkaido, Japan

AYUMU HAYASHI

Graduate School of Environmental Science, Hokkaido University, Hokkaido, Japan

(Manuscript received 26 August 2016, in final form 7 January 2017)

ABSTRACT

It has been revealed that in summertime, precipitation is enhanced to the south of the upper-level tropopause potential vorticity contours, which are accompanied by instantaneous jets, over the eastern coastal region of China to the northwestern Pacific. It is frequently exhibited as precipitation bands ranging in size from over a thousand to several thousands of kilometers long. In this study, an analysis was conducted to quantify the relationship depending on the phase of upper-level disturbances. With composite analysis, it is shown that the enhancement along the contours occurs at all phases; it occurs not only to the east but also to the west of the upper-level troughs, although it is weaker. The midtropospheric distributions of upwelling and the \mathbf{Q} -vector convergence are collocated with the precipitation enhancement, suggesting the importance of dynamical induction by geostrophic flow at all phases. The effects of upper-level disturbances and low-level jets (LLJs) with a southerly component are investigated by using an idealized nondimensional quasigeostrophic model supporting latent heating. While upper-level waves induce upwelling and downwelling to the east and west, respectively, of the upper-level troughs, LLJs tend to offset the downwelling, enabling precipitation to the west too. Both in the observational composite and the idealized model with LLJ, confluence and diffluence contribute to the \mathbf{Q} -vector convergence to induce upwelling along the subtropical jet irrespective of upper-level disturbance phases. This induction is explained as a general feature of a veered jet where geopotential isolines rotate clockwise with height without requiring wind variation along the jet.

1. Introduction

In summertime East Asia and the northwestern Pacific, moisture is provided from the tropics along the western and northern rim of the North Pacific high. Extensive studies have been conducted on mesoscale disturbances in this season, especially in the mei-yu–baiu period (Ninomiya and Akiyama 1992; Ninomiya and Shibagaki 2007, and the references therein). However, relatively few studies are made on the dynamics of synoptic features (e.g., Akiyama 1990; Chang et al. 1998).

Kodama (1993) conducted a study of summertime subtropical convergence zones, such as the mei-yu–baiu

frontal zone. He showed that satellite-derived cloudiness of high-level clouds, a proxy for precipitation, is enhanced when low-level (850 hPa) poleward wind and upper-level (300 hPa) westerly wind are enhanced.

Horinouchi (2014, hereinafter H14) studied summertime synoptic variability of precipitation and moisture transport at midlatitude from the eastern coastal region of China to the northwestern Pacific. A clear relationship was found between upper-tropospheric disturbances, which can be interpreted as Rossby waves, surface precipitation, and lower-tropospheric humidity in July and August. It was revealed that a precipitation band of several hundred kilometers wide and a thousand to several thousand kilometers long is formed frequently along (near and to the south of) the isentropic (350 K) and constant potential vorticity (1.5 or 3 PVU; $1 \text{ PVU} \equiv 10^{-6} \text{ K kg}^{-1} \text{ m}^2 \text{ s}^{-1}$) lines. More recently, Yokoyama et al. (2016, manuscript submitted to *J. Climate*) elucidated the types and sizes of the convective systems associated with this enhancement by using satellite radar data.

 Denotes content that is immediately available upon publication as open access.

Corresponding author e-mail: Takeshi Horinouchi, horinout@ees.hokudai.ac.jp

The finding by H14 is roughly consistent with Kodama (1993), since zonal winds are enhanced along the lines. Note that the 350-K isentropic surface is climatologically near the 200-hPa isobaric level nearly globally, and the 2-PVU constant potential vorticity (PV) roughly corresponds to the tropopause in the extratropics. Therefore, the isentropic constant-PV lines normally lie between tropospheric and stratospheric air masses at around 200 hPa, so they are sometimes referred to as tropopausal PV contours in what follows.

H14 revealed that the synoptic dynamical forcing is predominantly downward from upper-level Rossby waves that propagate along the subtropical Asian jet. The upper-level disturbances geostrophically induce upwelling and affect low-level horizontal moisture transport, both of which contribute to the formation of precipitation bands to the south of the lines.

The case studies of H14 demonstrated that precipitation is sometimes enhanced not only to the east of upper-level troughs, which is well explained by conventional synoptic meteorology, but also to the south or west of them. However, statistical and dynamical analysis of H14 did not discriminate such differences, so the phase-dependent structure is yet to be quantified.

In this study, composite analysis is made to elucidate the synoptic features of precipitation and associated quantities with respect to phases of upper-level disturbances. It is further studied how the enhancement along the upper-level isentropic constant-PV contours, or jets, occur broadly, even to the west of upper-level troughs.

The rest of this paper is organized as follows. Section 2 describes the data and methods used. Section 3 shows the results of composite analysis, and an interpretation is made in section 4 with a help of idealized model calculation. Conclusions are drawn in section 5.

2. Data and methods

a. Data

The data used in this study are version 7 of the Tropical Rainfall Measuring Mission (TRMM) Multisatellite Precipitation Analysis (TMPA) 3B42 product (Huffman et al. 2007), covering 50°S–50°N, for precipitation and the Japanese 55-year Reanalysis (JRA-55) for other quantities (Kobayashi et al. 2015). The periods used are June–September during 2001–2015; the results were similar if the months covered were shortened, for instance, to a single month of July.

The original resolution of the TMPA data is $0.25^\circ \times 0.25^\circ$, but it is coarsened to $0.5^\circ \times 0.5^\circ$ by binning. The horizontal resolution of JRA-55 data is $1.25^\circ \times 1.25^\circ$. The JRA-55 data are used at the original resolution for

parameters other than the geopotential height. Since the round-off error in the geopotential height data is severe for some quasigeostrophic (QG) analysis, it is smoothed by applying the 1–2–1 filter both in longitude and latitude and used at the resolution of $2.5^\circ \times 2.5^\circ$. Composite results in what follows are computed by using daily mean values. We checked some of the results with 6-hourly data, and the results were similar. The JRA-55 provides isentropic PV data computed on the model grid and sampled at the $1.25^\circ \times 1.25^\circ$ grid points. The data include small-scale features that are synoptically unimportant, such as filaments and isolated patches; note that the dynamical impact of PV anomalies is roughly limited by the Rossby scale height corresponding to horizontal scale. Therefore, a seven-point running mean, which is over the width of 10° , is applied with longitude to isentropic PV data before defining isentropic PV contours; no smoothing is applied with latitude in order not to change much the latitude where PV gradient is sharp in the meridional direction. No such smoothing is applied in H14, since it used the 2.5° NCEP data, and PV was computed from them in a diffusive manner by using central differentiation.

b. Composite analysis

As in H14, composite analysis is made by shifting target quantities (such as precipitation and specific humidity) meridionally with respect to the northernmost isentropic ($\theta = 350$ K, where θ is potential temperature) constant-PV (2 PVU) lines and averaging over time.¹ For each day d and longitude λ , the latitude of the contour $\varphi(\lambda, d)$ is derived, and the target quantities of the composite analysis are first interpolated meridionally to a grid of λ and $\delta\phi$, where $\delta\phi$ is the relative latitude with respect to the contour defined as $\delta\phi \equiv \phi - \varphi(\lambda, d)$, ϕ being latitude. Then the composites are derived as the time averages over selected days.

To elucidate phase dependence, days used to make composites are selected based on the mean latitudes of the line φ_0 , φ_1 , and φ_2 over longitudinal ranges 130° – 140° , 140° – 150° , and 150° – 160° , respectively, as demonstrated in Fig. 1:

- “Increasing” cases: $\varphi_0 < \varphi_1 < \varphi_2$ and $\varphi_2 - \varphi_0 > 4^\circ$
- “Decreasing” cases: $\varphi_0 > \varphi_1 > \varphi_2$ and $\varphi_0 - \varphi_2 > 4^\circ$
- “Flat” cases: $|\varphi_0 - \varphi_2| < 3^\circ$ and $|\varphi_1 - (\varphi_0 + \varphi_2)/2| < 3^\circ$

For all the composites, additional screening is applied as in H14 to select days where the northernmost contours

¹H14 used NCEP reanalysis data and chose 1.5-PVU contours to make composites. However, we chose 2-PVU contours in this study, since the 1.5-PVU contours in JRA-55 data are more discontinuous than those obtained from the NCEP data, and the locations of the JRA-55 2-PVU contours are generally close to those of the NCEP 1.5-PVU contours.

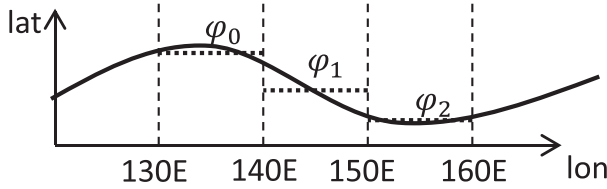


FIG. 1. Schematic illustration of the case selection in the composite analysis. The thick line shows an instantaneous (or daily mean) isentropic constant-PV line. This particular figure shows an example of a “decreasing” case.

are not discontinuous (latitudinal difference over zonally adjacent grid points is less than 10°) over 120°E–180° and that reside between 20° and 55°N (see H14 for more details). The composite results are shown over 115°–175°E. Where longitudinal dependence of composite results is briefly investigated, all the longitudinal ranges above are shifted uniformly.

The mean latitude of the northernmost 350-K 2-PVU contours for each composite, $\bar{\phi}_i$, is computed as a function of longitude, where the subscript i denotes symbolically one of the increasing, decreasing, and flat composite types. To visualize the dependence on the phase of upper-level disturbances, composite results obtained as functions of λ and $\delta\phi$ are relocated meridionally and shown as functions of λ and $\phi_r \equiv \delta\phi + \bar{\phi}_i(\lambda)$.

c. Idealized quasigeostrophic calculation

The quasigeostrophic potential vorticity (QGPV) equation is nondimensionalized assuming a constant Coriolis parameter (f plane) and the Boussinesq approximation as

$$\left(\frac{\partial}{\partial t} + u_g \frac{\partial}{\partial x} + v_g \frac{\partial}{\partial y}\right)q = \frac{\partial Q}{\partial z} \quad \text{and} \quad (1)$$

$$q \equiv 1 + \left(\frac{\partial^2}{\partial x^2} + \frac{\partial^2}{\partial y^2} + \frac{\partial^2}{\partial z^2}\right)\psi. \quad (2)$$

Here, t is nondimensional time normalized by $T \equiv f^{-1}$, where f is the Coriolis parameter; z is the nondimensional log-pressure height normalized by a height scale H , which is set equal to the tropopause height in the tropics; x and y are nondimensionalized by $L \equiv (NH)/f$, where N is the tropospheric buoyancy

frequency. The QGPV q and the QG streamfunction ψ are nondimensionalized by T and L , and $u_g \equiv -\partial\psi/\partial y$ and $v_g \equiv \partial\psi/\partial x$. Nondimensionalized diabatic heating Q is introduced to express condensation heating. As seen in Eq. (2), the Boussinesq approximation in this study is to neglect the factor of e^{-z} , which is proportional to pressure, as in the Eady problem (Eady 1949). The first term on the rhs of Eq. (2), 1, is the normalized Coriolis parameter. Typical dimensional values of the scaling parameters are $T = 1 \times 10^4$ s, $N = 0.01$ s⁻¹, $H = 10$ km, and $L = 1000$ km.

The QGPV inversion to solve Eq. (2) for ψ is conducted for specified q and boundary conditions. Diabatic heating Q is set to zero in the dry cases in what follows. In the moist cases, the nondimensional tropospheric static stability is reduced from 1 (dry value) to 0.25 where the vertical motion is upward; this parameter value choice is discussed in section 3, where composite equivalent potential temperature is investigated. This treatment is to crudely mimic the reduction of effective stability by latent heating. Vertical velocity $w \equiv Dz/Dt$ is obtained by solving the following nondimensional Boussinesq omega equation:

$$\left(\frac{\partial^2}{\partial x^2} + \frac{\partial^2}{\partial y^2} + \frac{\partial^2}{\partial z^2}\right)w = 2\left(\frac{\partial Q_1}{\partial x} + \frac{\partial Q_2}{\partial y}\right) + a\left(\frac{\partial^2}{\partial x^2} + \frac{\partial^2}{\partial y^2}\right)w, \quad (3)$$

where

$$(Q_1, Q_2) \equiv \left(\frac{\partial^2\psi}{\partial x\partial y} \frac{\partial^2\psi}{\partial x\partial z} - \frac{\partial^2\psi}{\partial x^2} \frac{\partial^2\psi}{\partial y\partial z}, \frac{\partial^2\psi}{\partial y^2} \frac{\partial^2\psi}{\partial x\partial z} - \frac{\partial^2\psi}{\partial x\partial y} \frac{\partial^2\psi}{\partial y\partial z}\right)$$

is the nondimensional and log-pressure version of the \mathbf{Q} vector by Hoskins et al. (1978); the last term on the rhs of Eq. (3) represents diabatic heating, so $a \equiv 0$ for dry cases, while in moist cases $a = 0.75$ where $w > 0$ in the troposphere and $a = 0$ elsewhere. Because of the nonlinearity through a , Eq. (3) is solved by iteration for the moist cases.

TWO-LATITUDINAL-BAND MODEL

The basic configuration of QGPV is set as follows:

$$q = \begin{cases} 1 & \text{if } y < 0 \text{ and } z < 1, \text{ or if } y > 0 \text{ and } z < 0.7, \\ 4 & \text{if } y < 0 \text{ and } z > 1, \text{ or if } y > 0 \text{ and } z > 0.7. \end{cases} \quad (4)$$

Here, the regions where $y < 0$ and $y > 0$ are meant to represent the tropics and extratropics, respectively, between which the tropopause height changes abruptly.

The boundary condition imposed is $u_g = 0$ at $y \rightarrow \pm\infty$ and $\psi' = 0$ at $z = 0$ and 2. Here, ψ' is the anomaly from the vertical profile of ψ at $y \rightarrow -\infty$, where ψ is a function

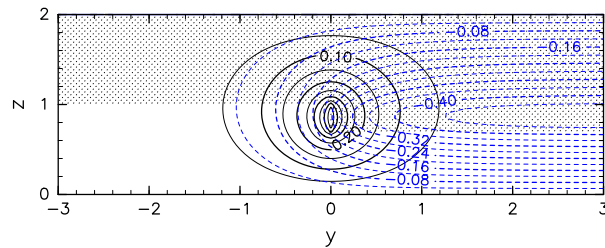


FIG. 2. Solution of the basic two-latitude band model: u_g (black solid contours) and ψ' (blue dashed contours). Stipples show the region where $q = 4$ (above $z = 1$ in the tropics and $z = 0.7$ in the extratropics).

only of z . The stratospheric q value of 4 is set to make it so that the squared static stability is $2^2 = 4$ times as large as in the troposphere.

Figure 2 shows the analytic solution for u_g and ψ' . There is a jet at $y = 0$, where u_g has a peak close to 0.5, which corresponds to 50 m s^{-1} if the typical scales above are assumed (note that $LT^{-1} = 100 \text{ m s}^{-1}$). Extratropical $\partial\psi'/\partial z$ is negative (positive) in the troposphere (stratosphere), indicating temperature is lower (higher) than in the tropics. Since this configuration is purely two-dimensional, $w = 0$ everywhere. In section 4, this basic model is modified to study the effects of upper-level waves and low-level jets.

3. Composite horizontal structures

Figure 3 shows the composite results for horizontal winds and geopotential height at 200 hPa. The numbers of days used for averaging are 389, 167, and 410 for the increasing, decreasing, and flat composites, respectively. The figure shows that instantaneous jets tend to reside around the 350-K 2-PVU contours, whose mean location is shown by red curves. This relationship is a consequence of the PV gap between the tropospheric and stratospheric air masses, as seen in Fig. 2.

Figure 4 shows that precipitation is concentrated around a few degrees to the south of the upper-level isentropic PV contours, as shown by H14. It further quantifies the phase dependence. Precipitation is enhanced to the east of the upper-level troughs, as expected from conventional synoptic meteorology. However, precipitation is enhanced along the PV contours at all phases, and it even occurs to the west of the upper-level troughs (Figs. 4a,b). Also, it occurs when the PV contours are relatively flat (Fig. 4c).

For comparison with the composite results, simple time mean precipitation is shown in Fig. 5a. The meridional distribution of the mean precipitation is much broader, and the peak value for each longitude is smaller than in the composites (Fig. 4). Although the

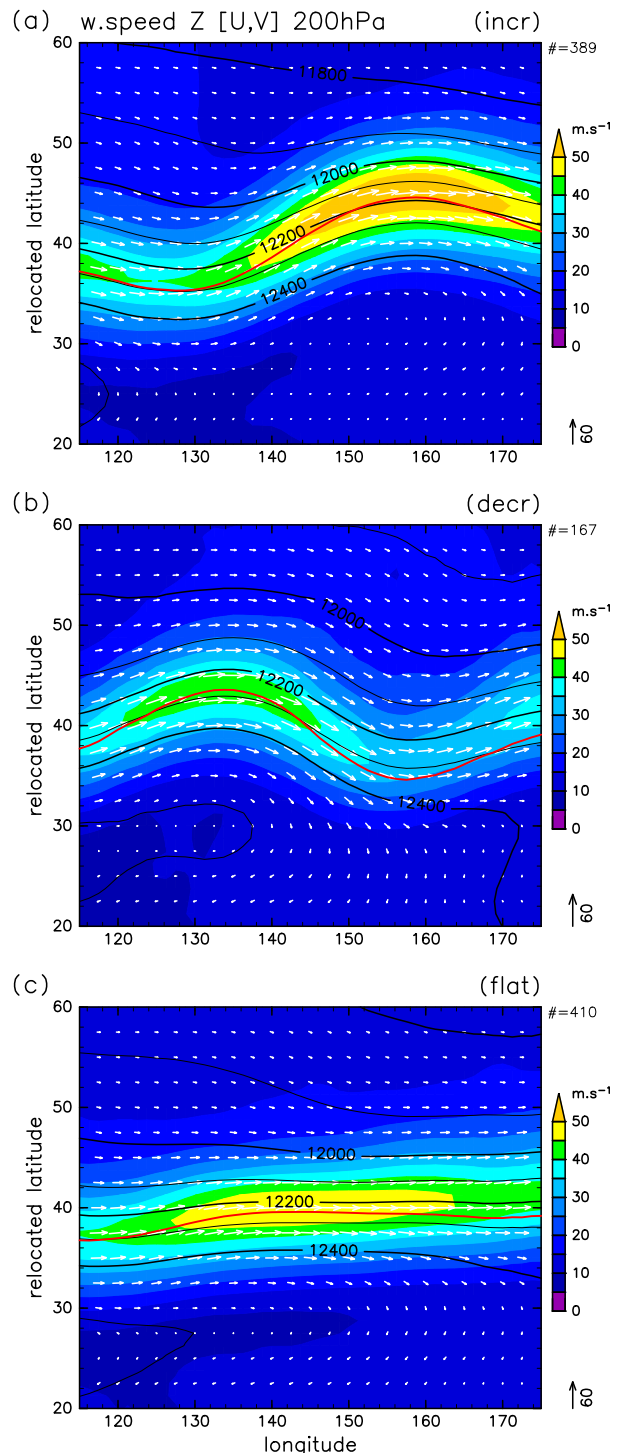


FIG. 3. The (a) increasing, (b) decreasing, and (c) “flat” composite horizontal wind vectors (arrows), horizontal wind speed (shading), and geopotential height [contours with values annotated (m)] at 200 hPa. The red curve in each panel shows $\bar{\phi}_i(\lambda)$, the mean latitude of the 350-K 2-PVU contours for each composite. For the composite quantities, the ordinate is the relocated latitude $\phi_r = \delta\phi + \bar{\phi}_i(\lambda)$. That is, time averages are meridionally shifted with respect to the red curves. The ordinate and the abscissa are scaled so that they are isotropic at 40° .

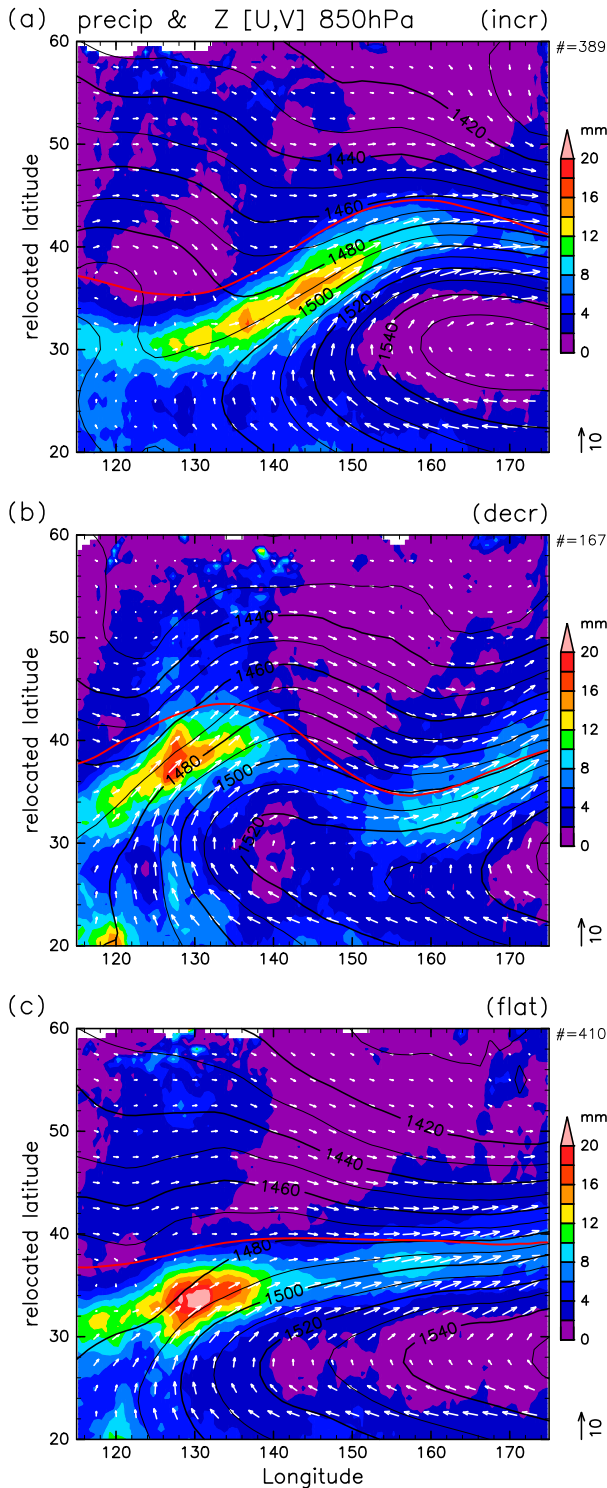


FIG. 4. As in Fig. 3, but showing composite precipitation (shading; mm day^{-1}) and 850-hPa horizontal winds and geopotential height.

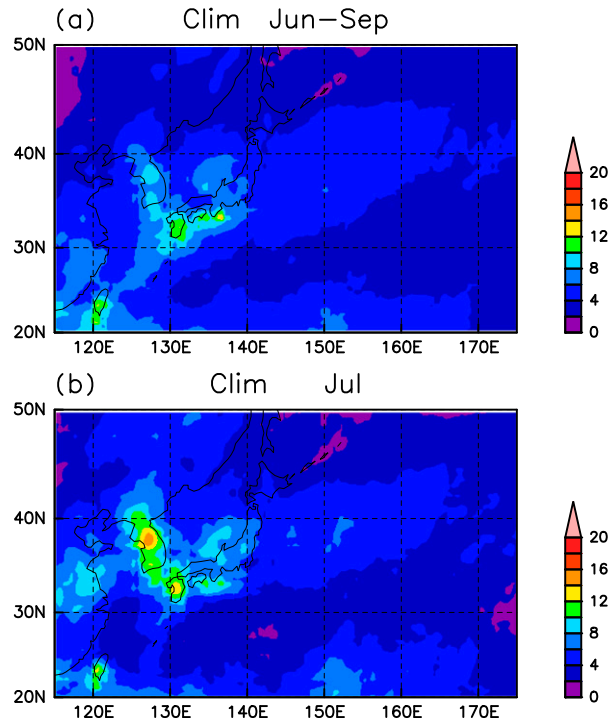


FIG. 5. (a) Mean precipitation averaged over June–September 2001–15 (mm day^{-1}). (b) As in (a), but for July only.

climatological distribution in Fig. 5a is smeared to some extent by the seasonal migration of precipitation, the climatology over a single month as in Fig. 5b is also meridionally broader than in Fig. 4. Therefore, the composite results suggest that precipitation is actually enhanced along the isentropic PV contours.

Low-level (850-hPa) geopotential height in Fig. 4 shows that the North Pacific high and hence the horizontal flow is modulated together with upper-level disturbances. Here, the causality should be predominantly downward as shown by H14. The precipitation enhancement is accompanied with the enhancement of low-level flows. This feature is consistent with earlier studies that have shown the importance of low-level jets for the precipitation along the mei-yu-bai frontal zones (e.g., Akiyama 1973; Chen and Yu 1988; Nagata and Ogura 1991). Note that the low-level flow enhancement to the east of upper-level troughs occurs near the entrance region of the 200-hPa jet (Fig. 3; the situation is similar at lower levels such as 300 and 400 hPa; not shown), so the mechanism working here is different from the low-level poleward flow enhancement at the exit region of jets suggested by Uccellini and Johnson (1979). It rather appears consistent with Chou et al. (1990), who showed the importance of diabatic heating and the angular momentum advection from lower latitude in the course of upper-level induced low-level frontogenesis.

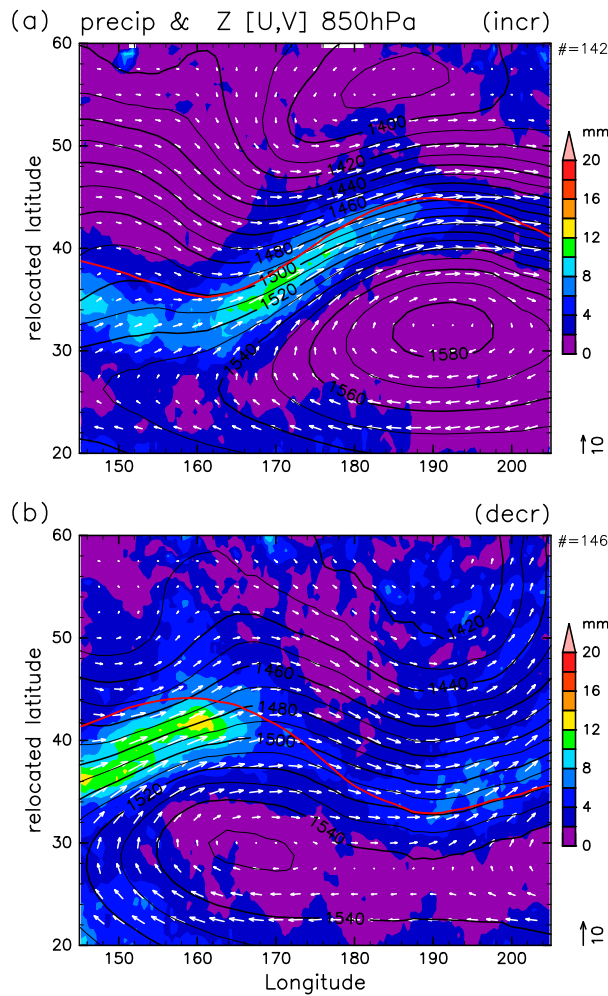


FIG. 6. As in Fig. 4, but the longitudinal ranges for composite and plot are shifted eastward by 30°. The flat composite is omitted for brevity.

This mechanism is also consistent with H14, who showed that surface fronts tend to reside a few hundred kilometers to the south of the upper-level 350-K 1.5-PVU contours.

Figures 4b and 4c show a large composite precipitation rate (around 20 mm day⁻¹) at around 130°E. It is associated with the relatively large climatological precipitation over the Korean peninsula and western Japan (see coast lines shown in Fig. 5). In order to further see the longitudinal dependence, the composite analysis is conducted by shifting the region longitudinally. Figure 6 is an example, where it is shifted eastward by 30°. The result is qualitatively similar to Figs. 4a and 4b. The overall smallness can be explained in terms of the smallness of the climatological precipitation. Similar relationship between the upper-level isentropic PV contours and precipitation are found over the western to central Pacific

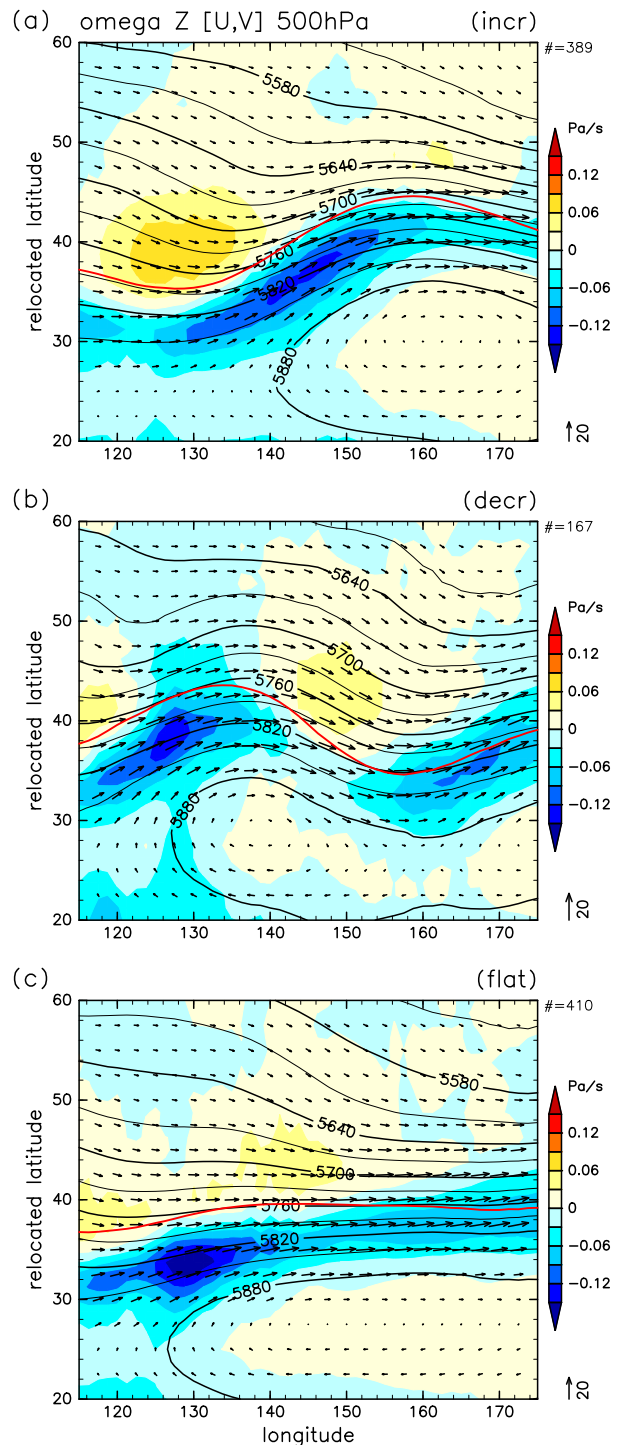


FIG. 7. As in Fig. 3, but showing results for 500 hPa and with shading showing the vertical pressure velocity.

and over the Atlantic (not shown), where precipitation is relatively large.

The distribution of precipitation in Fig. 4 is quite similar to that of vertical motion (Fig. 7) and the

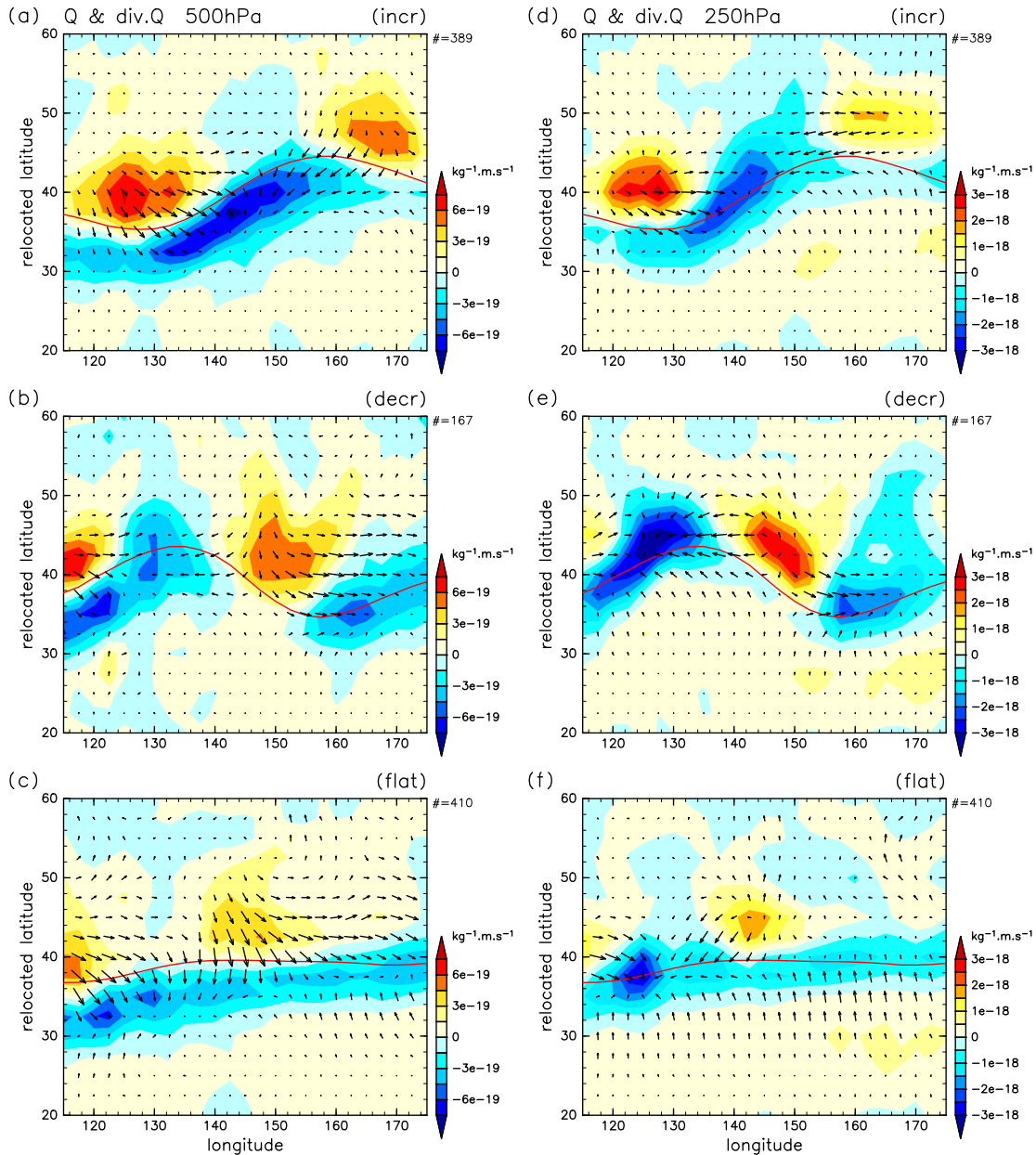


FIG. 8. As in Fig. 3, but with arrows showing the \mathbf{Q} vector and shading showing its divergence at (a)–(c) 500 and (d)–(f) 250 hPa.

convergence of the \mathbf{Q} vector (Figs. 8a–c) at 500 hPa. This result suggests that precipitation is induced (or initiated) by the secondary circulation associated with geostrophic flow, although, in terms of strength, the effect of latent heating should be important. Note that the \mathbf{Q} -vector divergences to the west of upper-level troughs are situated northward of the red curves at both 500 and 250 hPa (Fig. 8). Therefore, if zonal averaging is made along fixed relative latitude $\delta\phi$, convergence remains at around and to the south

of the isentropic constant-PV contours (zero to small negative $\delta\phi$).

The \mathbf{Q} -vector component parallel to temperature gradient is associated with confluence (when upgradient) or diffluence (when downgradient) along the direction of the gradient, and the \mathbf{Q} -vector component perpendicular to temperature gradient is associated with the rotation of temperature isolines, which leads to shear deformation (Hoskins et al. 1978). The \mathbf{Q} -vector divergences shown in Figs. 8a and 8b are separated into the contributions

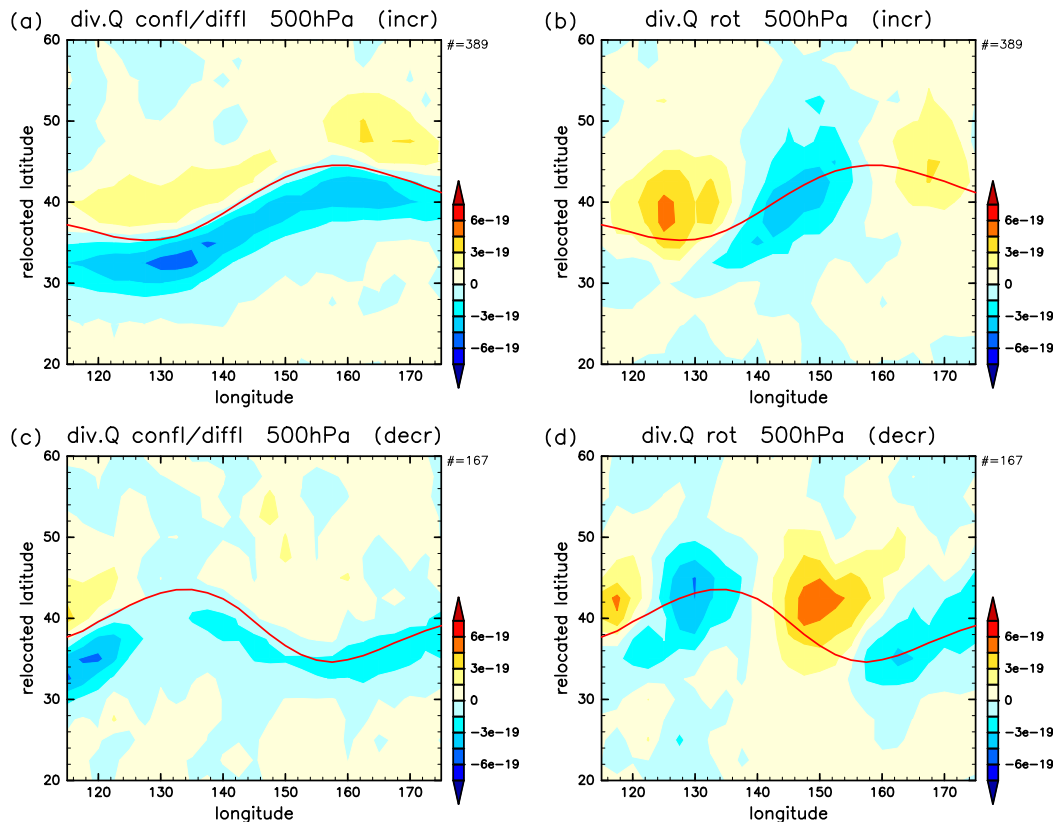


FIG. 9. Composite \mathbf{Q} -vector divergence at 500 hPa in which (a),(c) the confluence/diffuence contribution and (b),(d) the rotational (or shear-deformation) contribution are separated. Only the results for the (a),(b) increasing and (c),(d) decreasing composites are shown for brevity.

associated with confluence/diffuence and shear deformation for each day, and a composite is made afterward for each contribution. Figure 9 shows the result. The numerical method of the separation is described in the appendix.

Figures 9a and 9c show that the \mathbf{Q} -vector convergence associated with confluence/diffuence is distributed all along the isentropic PV contours. Therefore, the confluence/diffuence contribution is important for the overall precipitation enhancement along the isentropic PV contours. The cause of confluence/diffuence is revisited in section 4. On the other hand, both convergence and divergence are seen in the rotational contribution shown in Figs. 9b and 9d. Its distribution is consistent with the well-known synoptic feature that the convergence (divergence) is present to the east (west) of the upper-level troughs. Therefore, the phase dependence shown above is mainly associated with shear deformation. The result is consistent with H14, which showed the importance of confluence/diffuence of temperature isolines in the composite without discriminating the phase of upper-level disturbances.

Composite moist stability is examined by using Fig. 10. Color shading in it shows the difference between the saturation equivalent potential temperature θ_e^* at 500 hPa

and the equivalent potential temperature θ_e at 925 hPa (negative value indicates unstable condition). The stability is modulated with the upper-level disturbances. It is increased with latitude up to the PV contours, so the precipitation belts shown in Fig. 4 are less favorable for penetrative convection than at lower latitude, which indicates the importance of large-scale dynamical induction. Note that the zonal contrast to the north of 40° in the figure is mainly due to the low-level temperature difference between land and ocean (see Fig. 5 for land distribution).

Figure 10 indicates that the composite $\theta_e^*(500 \text{ hPa}) - \theta_e(925 \text{ hPa})$ is 5–10 K where precipitation is enhanced. The composite (dry) potential temperature difference (not shown) is around 30 K. Therefore, the effective moist stability is 1/3–1/6 of the dry stability in a crude sense, which is why the nondimensional effective stability is set to an intermediate value of 0.25 (see section 3c).

Figure 11 shows the composite precipitation for the “decreasing” cases with an additional restriction: cases are limited to when the precipitation averaged over $-10^\circ < \delta\phi < 0^\circ$ and $130^\circ < \lambda < 150^\circ\text{E}$: that is, precipitation near and to the south of the PV contour and to the

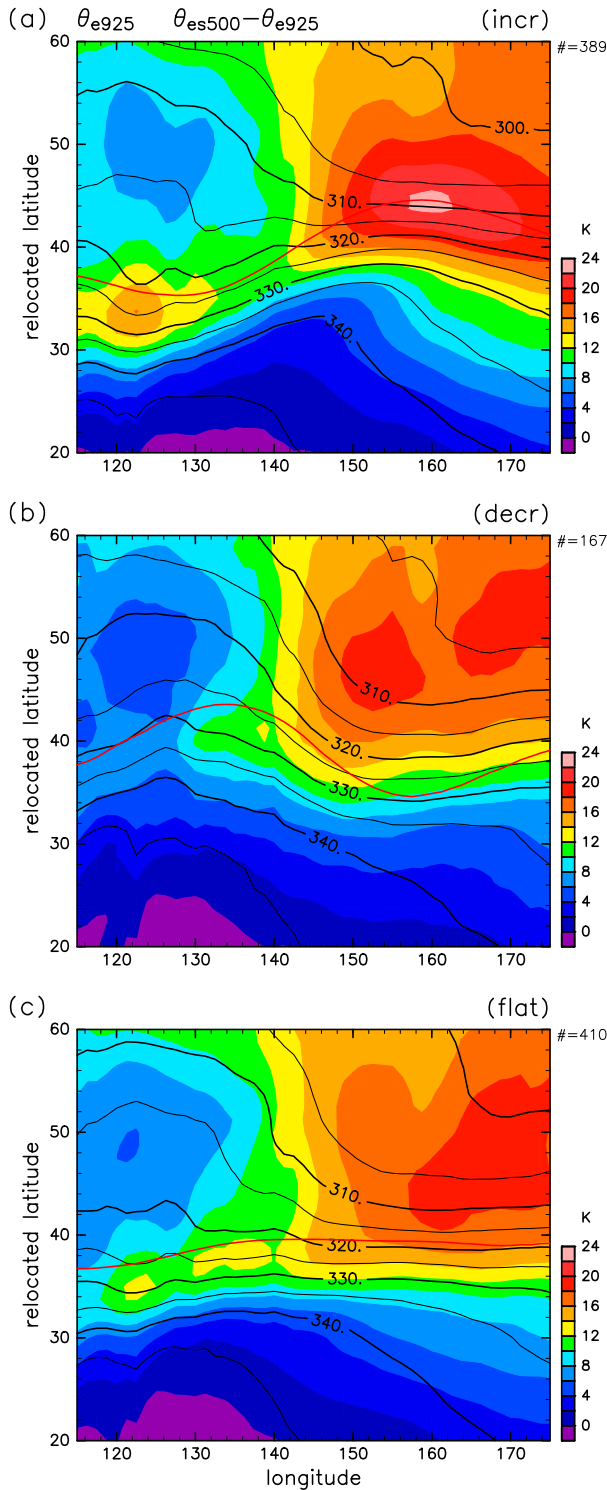


FIG. 10. As in Fig. 3, but for $\theta_e^*(500 \text{ hPa}) - \theta_e(925 \text{ hPa})$ (shading) and $\theta_e(925 \text{ hPa})$ (contours).

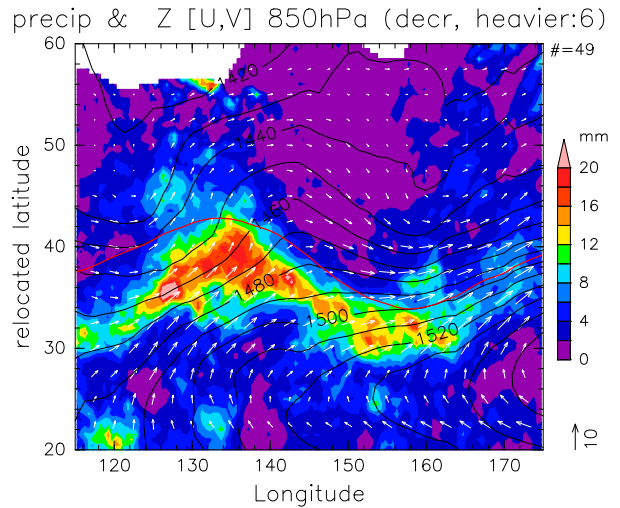


FIG. 11. As in Fig. 4b, but cases are limited to when the precipitation averaged over $-10^\circ < \delta\phi < 0^\circ$ and $130^\circ < \lambda < 150^\circ\text{E}$ is greater than 6 mm day^{-1} .

west of upper-level trough, is greater than 6 mm day^{-1} . The number of the cases used is 49. The low-level jet in this composite is situated more southward than in the standard “decreasing” composite shown in Fig. 4b. Since the low-level flow is not perfectly correlated with upper-level disturbances, there is some fluctuation in their relationship, and the present result indicates that precipitation to the west of the upper-level trough is enhanced when low-level flow impinges on where the tropopausal PV contours run northwest–southeast.

4. Effect of upper-level disturbances and low-level jets

The simple zonally symmetric two-latitude-band model defined in section 2 is modified to include upper-level waves by shifting the boundary between the tropopausal q gap over $0.7 < z < 1$ to $y = 0.3 \sin(2\pi x/3)$ for $|x| < 1.5$, as shown by the red curve in Fig. 12. This case is referred to as case 1 in what follows. Note that this structure is not steady, so it is meant to represent an instantaneous feature. The QGPV inversion to solve Eq. (2) is conducted by numerically integrating the horizontal Green function for the difference from the zonally symmetric case. The computational resolution is 0.05 in all directions. The solution at $z = 0.85$ is shown in Fig. 12a. As in the zonally symmetric case, the q boundary (red curve) is accompanied by a jet.

Secondary circulation exists for this zonally asymmetric q distribution. Figure 12b shows the \mathbf{Q} vector and its divergence in the midtroposphere ($z = 0.5$). As expected, both positive and negative divergence is found according to the direction of the red curve in the x – y plane (e.g., it is positive where the curve is running northwest–southeast).

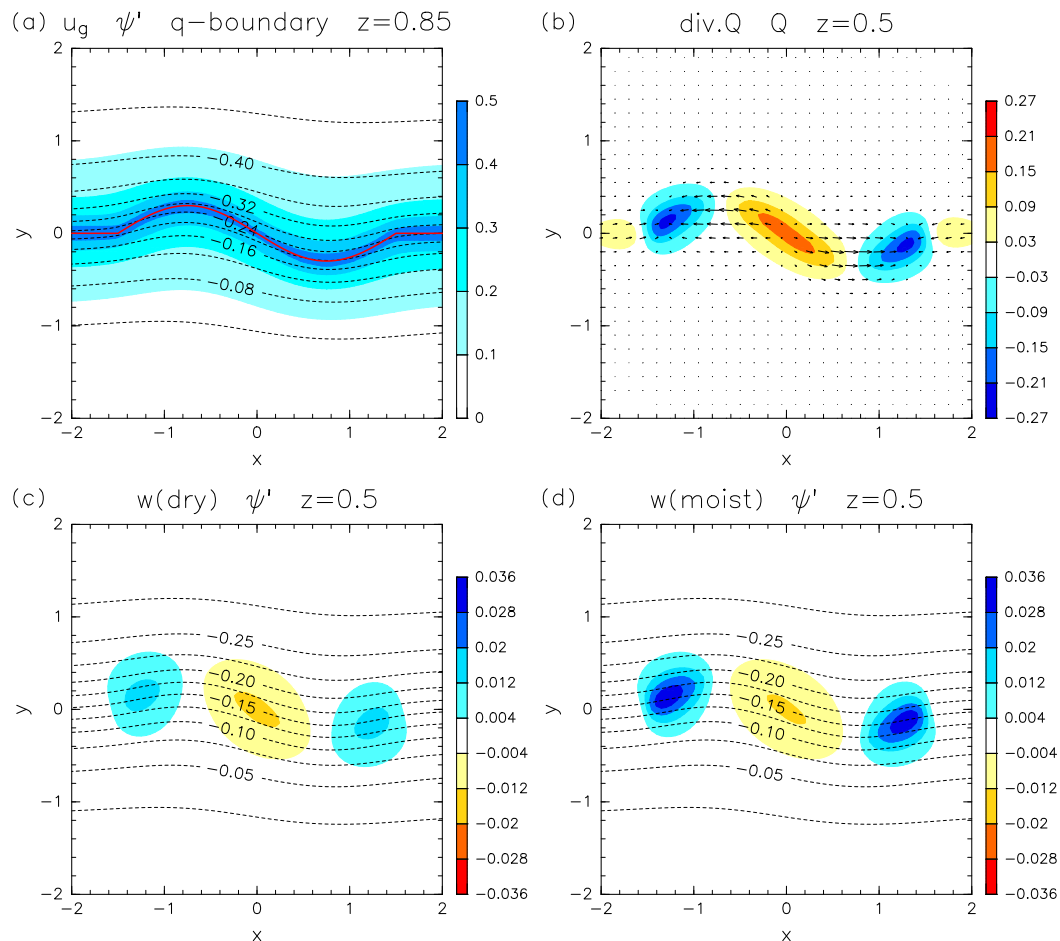


FIG. 12. Solution of case 1, having a wavy upper-level stratosphere–troposphere boundary. (a) The ψ' (contours) and u_g (shading) at $z = 0.85$. The red curve shows the boundary between the regions with $q = 4$ (to the north; stratospheric air mass) and $q = 1$ (to the south; tropospheric air mass) over $z = 0.7$ – 1 . (b) The \mathbf{Q} vector (arrows) and its divergence (shading) at $z = 0.5$. (c) The dry solution of w (shading) and ψ' (contours) at $z = 0.5$. (d) As in (c), but for the moist solution of w (shading).

Accordingly, both upwelling and downwelling are found in the dry solution of w (Fig. 12c). Since the omega equation [Eq. (3)] is elliptic, w is more spread than the \mathbf{Q} -vector divergence. The effect of latent heating acts to strengthen and concentrate upwelling (Fig. 12d). It is interesting that the horizontal extent of upwelling is similar to that of the \mathbf{Q} -vector convergence, as in Figs. 7 and 8. The downwelling at around $x = y = 0$ suggests that the upper-level wave alone does not induce precipitation all along the tropopausal PV contours.

As shown in section 3, there is an enhancement of low-level flows associated with upper-level disturbances. Here, we examine its effect by adding a low-level jet (LLJ) to the idealized model. To crudely mimic an LLJ, a QG streamfunction anomaly, ψ'_l , is added to case 1, which is called case 2 in what follows.

Here, ψ'_l is two-dimensional, varying only with z and $r \equiv y \cos \alpha - x \sin \alpha$, where α is set to 20° . The anomaly has zero QGPV, so $[(\partial^2/\partial r^2) + (\partial^2/\partial z^2)]\psi'_l = 0$. To represent an LLJ, $\psi'_l(r, z)$ at the bottom is varied as $\psi'_l(r, 0) = -0.15 \tanh(1.5r)$, while it is set to zero at the top boundary. The total ψ' of case 2 is shown in Fig. 13 for $z = 0.1$ (Fig. 13a) and $z = 0.5$ (Figs. 13c,d); ψ'_l alters the total ψ' mainly near the bottom. However, the existence of the LLJ alters the \mathbf{Q} -vector divergence and w widely over z . Whether w is negative or positive around $x = y = 0$ depends on the strength and width of the LLJ, but it generally decreases the \mathbf{Q} -vector divergence and increases w , whether dry or moist, from no-LLJ cases (case 1).

The \mathbf{Q} -vector divergence is divided into the components parallel and perpendicular to the horizontal temperature gradient, and the results at $z = 0.5$ are shown in

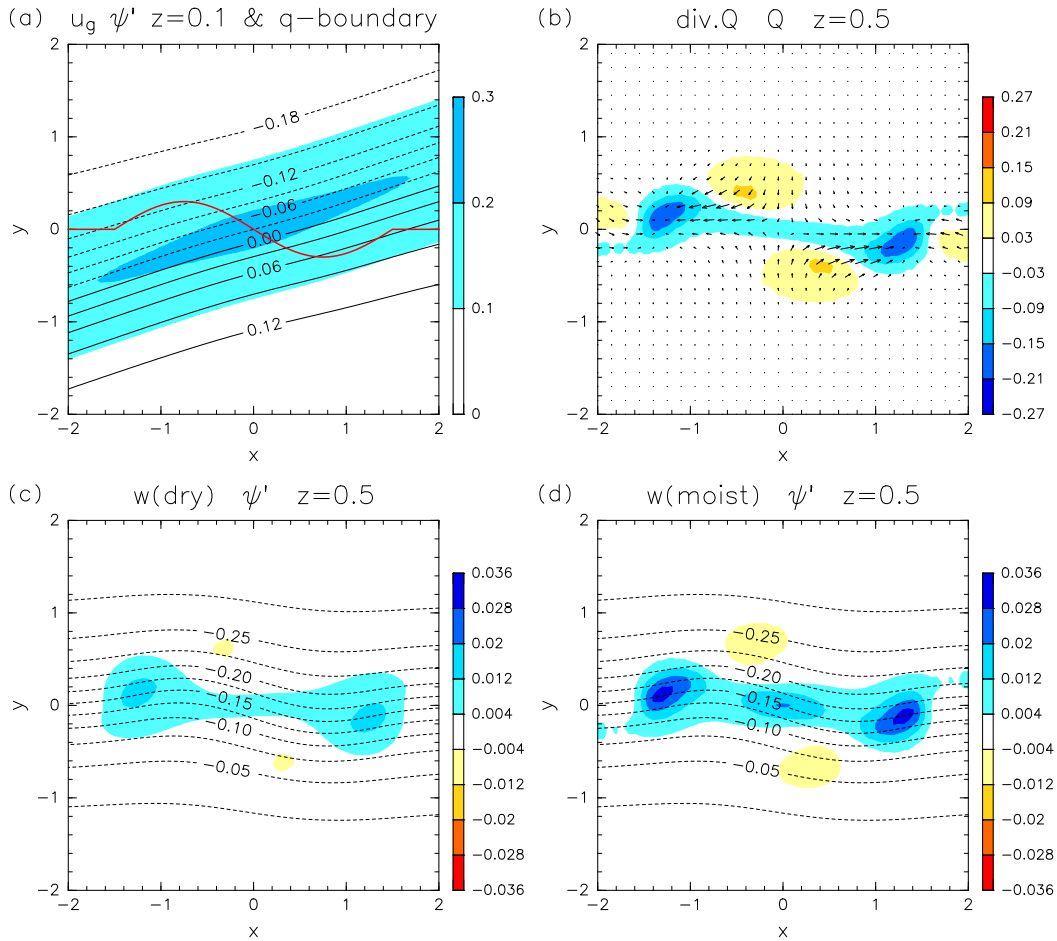


FIG. 13. As in Fig. 12, but for case 2, which has a low-level jet, and in (a) ψ' and u_g are shown for $z = 0.1$.

Fig. 14. As expected, the total divergence in case 1 (Fig. 13b) is mainly attributed to the perpendicular component (Fig. 14b) that express the effect of the rotation of temperature isolines, or shear deformation. In case 2 (with an LLJ), the rotational contribution (Fig. 14d) to the positive divergence at around $x = y = 0$ is weaker than in case 1 (Fig. 14b). Also, the contribution of confluence/diffuence is prominent, producing the \mathbf{Q} -vector convergence along the subtropical jet, which is enhanced to the west of the upper-level trough (bluish region around $x = y = 0$ in Fig. 14c). The resemblance of the idealized model results and the composite results suggests that the model captures the basic features of the observed precipitation enhancement.

The effect of LLJ on the \mathbf{Q} -vector convergence along the upper-level jet is explained as follows. Since the tendency by the QG horizontal temperature advection $-u_g(\partial T/\partial x) - v_g(\partial T/\partial y)$ is proportional to

$$\frac{\partial \psi}{\partial y} \frac{\partial^2 \psi}{\partial x \partial z} - \frac{\partial \psi}{\partial x} \frac{\partial^2 \psi}{\partial y \partial z},$$

it is positive when ψ contours rotate clockwise with height, which is called veering. As seen from Figs. 13a and 13c, the introduction of an LLJ creates veered environment, providing warm horizontal advection. Therefore, w is likely positive in a crude sense, but the observed concentration of the \mathbf{Q} -vector convergence along jet needs further explanation.

For the explanation, we introduce a Cartesian r - s coordinate where the r (s) axis is perpendicular (parallel) to temperature gradient as in Fig. 15. The \mathbf{Q} -vector components in this coordinate are

$$\begin{aligned} (Q_r, Q_s) &\equiv \left(-\frac{\partial^2 \psi}{\partial r^2} \frac{\partial^2 \psi}{\partial s \partial z}, -\frac{\partial^2 \psi}{\partial r \partial s} \frac{\partial^2 \psi}{\partial s \partial z} \right) \\ &= \left(-\frac{\partial v_s}{\partial r} \frac{\partial T}{\partial s}, -\frac{\partial v_s}{\partial s} \frac{\partial T}{\partial s} \right), \end{aligned}$$

where $v_s \equiv \partial \psi / \partial r$ is the geostrophic wind along the s axis and $T \equiv \partial \psi / \partial z$ corresponds to temperature. The confluence/diffuence contribution to the \mathbf{Q} -vector divergence is expressed as

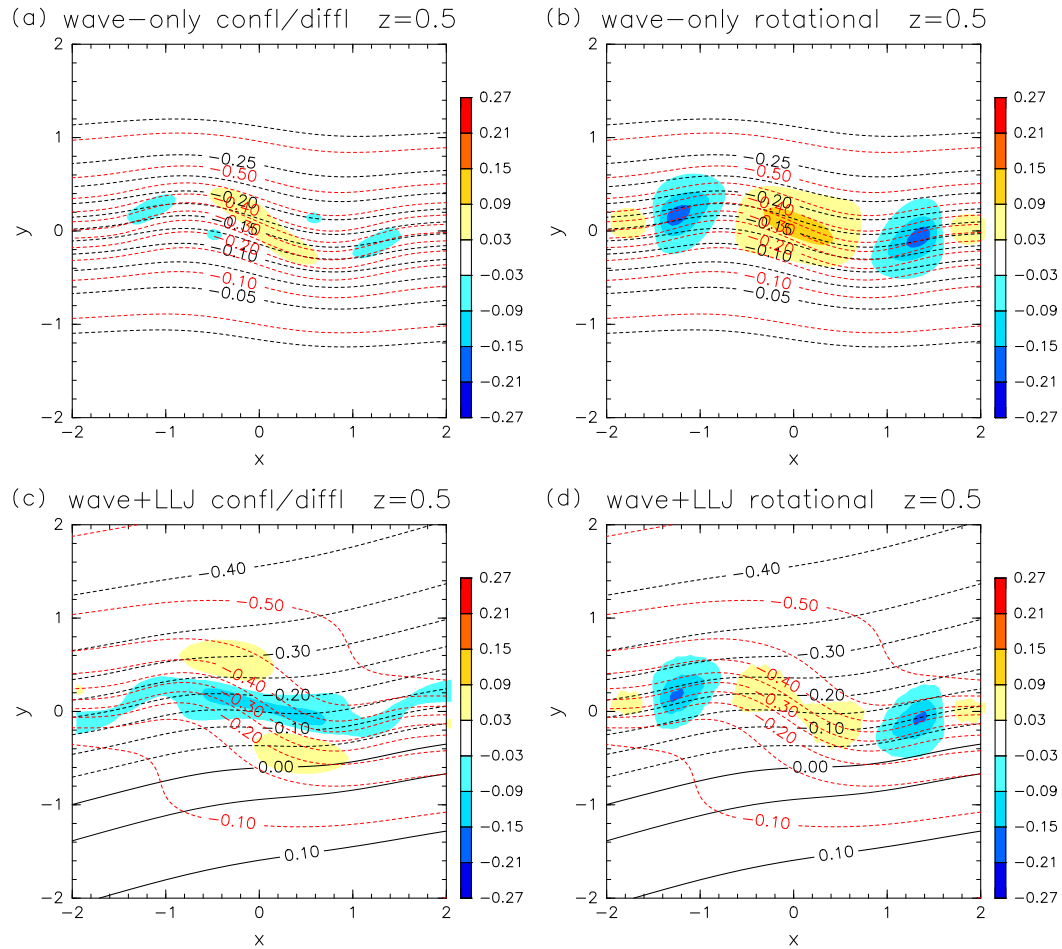


FIG. 14. Color shading: (a),(c) confluence/diffusion contributions and (b),(d) rotational (or shear-deformation) contributions to nondimensional \mathbf{Q} -vector divergence at $z = 0.5$ for (a),(b) case 1 and (c),(d) case 2. Black contours: ψ at $z = 0.5$ for (a),(b) case 1 and (c),(d) case 2. Red contours: the same, but for $\partial\psi/\partial z$.

$$\frac{\partial Q_s}{\partial s} = -\frac{\partial^2 v_s}{\partial s^2} \frac{\partial T}{\partial s} - \frac{\partial v_s}{\partial s} \frac{\partial^2 T}{\partial s^2}. \quad (5)$$

The effect of the first term on the rhs is illustrated in Fig. 15. It is negative (convergent) along the axis of the jet flowing downgradient of temperature (here, $\partial T/\partial s > 0$, $v_s < 0$, and $\partial^2 v_s/\partial s^2 > 0$). The \mathbf{Q} -vector convergence in Fig. 14c is explained by this effect. The second term on the rhs of Eq. (5) is not significant.

Figure 15 also illustrates that the rotational contribution ($\partial Q_r/\partial r$) is also convergent. The difference between Fig. 14b and Fig. 14d at around $x = y = 0$ is mainly attributed to this effect. The relative importance among $\partial Q_s/\partial s$ and $\partial Q_r/\partial r$ depends on the angle of the jet: the shallower the jet axis direction is with respect to temperature isolines, the greater is the contribution of $\partial Q_s/\partial s$.

Veering (clockwise rotation of the geopotential height contours with height) is also seen in the

observational composite by comparing Fig. 4 (850 hPa), Fig. 7 (500 hPa), and Fig. 3 (200 hPa). The \mathbf{Q} -vector convergence due to confluence/diffusion (Figs. 9a,c) occurs where horizontal wind is strong (Fig. 7) and temperature gradient is relatively large (not shown), suggesting that the first term of the rhs of Eq. (5) is also important as in the idealized model.

Quantitatively, there are differences between the idealized model results and observational composite results, as a matter of course. In the composite results, precipitation is enhanced to the south of, not directly underneath, the upper-level tropopause PV contours. This shift does not occur in the present QG model. The discrepancy is presumably due to the lack of the semigeostrophic effect in the QG model, as has been pointed out in the context of frontogenesis (e.g., Hoskins 1982). The southward shift is relatively greater to the west of 140°E . That may be because the region corresponds to the western periphery of the

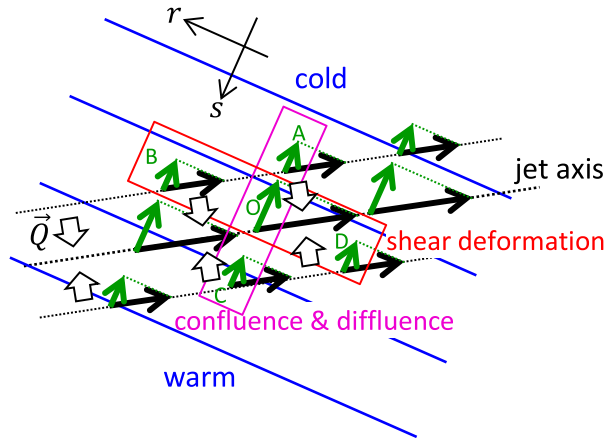


FIG. 15. Schematic illustration of the \mathbf{Q} -vector convergence along the jet that flows downgradient of temperature. Blue lines: temperature isolines. Black dotted lines: stream lines, where the middle one represents the jet axis. Black arrows: horizontal wind vectors associated with the jet. Green arrows: horizontal wind components parallel to temperature gradient (here referred to as along-gradient winds). Bold outlined arrows: \mathbf{Q} vectors, which converge along the jet. The along-gradient wind vectors A, O, and C (in the purple rectangle) exemplify the confluence (between A and O) and diffuence (between O and C) associated with the nonuniformity of winds along temperature gradient. The along-gradient wind vectors B, O, and D (in the red rectangle) exemplify the shear deformation associated with the nonuniformity along temperature isolines. The \mathbf{Q} -vector convergence is due to both the confluence/diffuence and the shear deformation.

North Pacific high, so a mid- to low-level jet is climatologically confluent. As is well known, the jet entrance region induces upwelling to its warmer (here, southern) side; if the wind speed increases downwind of the jet in Fig. 15, the confluent up-temperature-gradient \mathbf{Q} -vector component is increased, and the \mathbf{Q} -vector convergent region is shifted to the warmer side.

5. Conclusions

It has been revealed that, in summertime, precipitation is enhanced to the south of the upper-level tropopausal PV contours over the eastern coastal region of China to the northwestern Pacific. In this study, further analysis was made to elucidate the synoptic features of precipitation and associated quantities in relation to the phases of upper-level disturbances.

The composite analysis showed that precipitation is enhanced to the east of the upper-level trough, as expected, and it further revealed that precipitation is enhanced along the isentropic PV contours at all phases, even to the west of the upper-level troughs. Where precipitation is enhanced, not only upwelling but also the

\mathbf{Q} -vector convergence is enhanced in the midtroposphere, suggesting that moist convection is predominantly induced dynamically by geostrophic flow, while it is enhanced by latent heat release. The \mathbf{Q} -vector convergence was separated into the contributions associated with confluence/diffuence (owing to the \mathbf{Q} -vector component parallel to the horizontal temperature gradient) and shear deformation (owing to the \mathbf{Q} -vector component perpendicular to it), and a composite was made for each contribution. The result showed that \mathbf{Q} -vector divergence associated with confluence/diffuence is negative (convergent) all along the isentropic PV contours, suggesting its importance in the enhancement of precipitation along the contours.

The importance of the dynamical induction of upwelling is also supported by the analysis of moist stability. The precipitation enhancement is accompanied by the enhancement of southwesterly low-level flow, or LLJs. The importance of LLJs is also suggested by a composite for cases where precipitation is especially enhanced to the west of upper-level troughs.

The effect of upper-level disturbances and LLJs on vertical motion was investigated by using a non-dimensional QGPV inversion of idealized geostrophic distributions. As expected, upper-level waves induce upwelling and downwelling to the east and west, respectively, of the upper-level trough, which is primarily associated with shear deformation. Condensation heating strengthens and concentrates upwelling, but upper-level waves alone do not explain the precipitation enhancement all along the tropopausal PV contours, since downwelling remains. Inclusion of a southwesterly LLJ to the idealized model alters the distribution of the \mathbf{Q} -vector convergence and upwelling, reducing the downwelling to the west of upper-level troughs, even creating upwelling, depending on its strength, which is consistent with the composite results.

The effect of the inclusion of LLJ is explained as follows. Since it has a southerly component, the low-level geopotential has a positive eastward gradient. Therefore, the geopotential contours rotate clockwise with height, which is called veering. The veered geopotential structure indicates positive horizontal temperature advection, which is generally favorable for the formation of upwelling. Moreover, warm advection in the form of a jet provides confluence/diffuence and shear deformation that create \mathbf{Q} -vector convergence along the jet axis. Note that the confluence/diffuence associated with the jet does not require wind speed variation along the jet such as the “entrance” and “exit” features. The similarity of the idealized model

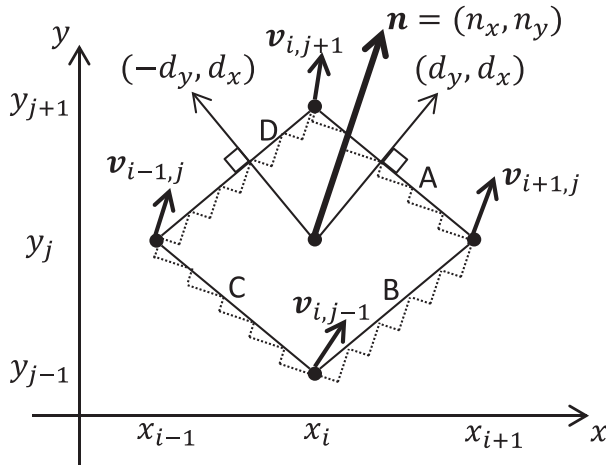


FIG. A1. Schematic diagram to help with the explanation of directional separation of divergence. See the appendix. The symbols A, B, C, and D denote the four sides of the rhombus.

result and observational composite suggests that the model captures basic features of the precipitation enhancement along tropopausal isentropic PV contours, or jets.

The main difference between the observational composite and idealized model is that precipitation is enhanced to the south of the upper-level tropopausal PV contours, while it is directly underneath in the idealized model. It is speculated that it is partly because of the lack of the semigeostrophic effect in the model. Also, the dominance of confluence in the mid to lower troposphere corresponding to the western periphery of the North Pacific high may be another factor.

Horizontal temperature advection is treated as an indicator of vertical motion in climate studies such as Rodwell and Hoskins (1996) and Sampe and Xie (2010). From the present study, it can be further argued that not only warm advection (or veering) but also the existence of jet there should be important for the climatology of precipitation zones.

Acknowledgments. We thank Drs. Yukari Takayabu, Chie Yokoyama, and Atsushi Hamada for helpful discussion on this study. We also thank the two anonymous reviewers for helpful comments, which improved the manuscript significantly. This study was partially supported by the Environment Research and Technology Development Fund (2-1503) of the Ministry of the Environment, Japan, and by the Japan Society for the Promotion of Science (JSPS) Grant 16K05550.

APPENDIX

A Four-Point Formula to Separate Directional Contributions to Two-Dimensional Divergence

In this study, \mathbf{Q} -vector divergence is separated into contributions parallel and perpendicular to the horizontal temperature gradient as in Figs. 9 and 14. It is numerically conducted by using the four-point formulation described in what follows.

Imagine an arbitrary two-dimensional vector field $\mathbf{v} \equiv (u, v)$ as a function of x and y with divergence $D \equiv \partial u/\partial x + \partial v/\partial y$. As illustrated in Fig. A1, vector fields are sampled at equally separated grid points at $x = x_i$ and $y = y_j$, where i and j are integers; $x_{i+1} - x_i = d_x$, and $y_{j+1} - y_j = d_y$. We define the horizontal gradient of temperature, ∇T , at (x_i, y_j) by using the central differentiation as $\nabla T_{i,j} = [(T_{i+1,j} - T_{i-1,j})/(2d_x), (T_{i,j+1} - T_{i,j-1})/(2d_y)]$, where the subscript i, j represents a quantity at (x_i, y_j) . A unit vector $\mathbf{n} = (n_x, n_y)$ is defined as $\nabla T_{i,j}/|\nabla T_{i,j}|$, and another unit vector $\mathbf{n}_\perp = (n_y, -n_x)$ is introduced. The present task is to separate $D_{i,j}$ into the contributions parallel and perpendicular to \mathbf{n} , which are expressed as $D_{\parallel i,j}$ and $D_{\perp i,j}$, respectively. Note that the nonuniformity of \mathbf{n} is neglected as being secondary (it converges to zero when $d_x \rightarrow 0$ and $d_y \rightarrow 0$).

Supposing that \mathbf{v} varies linearly along each of the four sides of the rhombus in Fig. A1 and dividing the net outflow with the area $2d_x d_y$, a discrete form of divergence is derived as

$$\begin{aligned}
 D_{i,j} &= \frac{\mathbf{d} \cdot \frac{\mathbf{v}_{i,j+1} + \mathbf{v}_{i+1,j}}{2} - \mathbf{d} \cdot \frac{\mathbf{v}_{i-1,j} + \mathbf{v}_{i,j-1}}{2} + \mathbf{e} \cdot \frac{\mathbf{v}_{i,j+1} + \mathbf{v}_{i-1,j}}{2} - \mathbf{e} \cdot \frac{\mathbf{v}_{i+1,j} + \mathbf{v}_{i,j-1}}{2}}{2d_x d_y} \\
 &= \frac{u_{i+1,j} - u_{i-1,j}}{2d_x} + \frac{v_{i,j+1} - v_{i,j-1}}{2d_y},
 \end{aligned} \tag{A1}$$

where $\mathbf{d} \equiv (d_y, d_x)$ and $\mathbf{e} \equiv (-d_y, d_x)$. The first to fourth terms of the numerator on the rhs of the first line of Eq. (A1) represent the outflux through the sides A, C, D, and B of the rhombus, respectively. The second line of the

equation indicates that this formulation of numerical divergence is the same as the simple one based on central differentiation.

Likewise, the directional separation is made as follows:

$$D_{\parallel ij} = \frac{(\mathbf{d} \cdot \mathbf{n}) \left(\mathbf{n} \cdot \frac{\mathbf{v}_{ij+1} + \mathbf{v}_{i+1j} - \mathbf{v}_{i-1j} - \mathbf{v}_{ij-1}}{2} \right) + (\mathbf{e} \cdot \mathbf{n}) \left(\mathbf{n} \cdot \frac{\mathbf{v}_{ij+1} + \mathbf{v}_{i-1j} - \mathbf{v}_{i+1j} - \mathbf{v}_{ij-1}}{2} \right)}{2d_x d_y}$$

$$= \frac{n_x^2(u_{i+1j} - u_{i-1j})}{2d_x} + \frac{n_y^2(v_{ij+1} - v_{ij-1})}{2d_y} + n_x n_y \left(\frac{v_{i+1j} - v_{i-1j}}{2d_x} + \frac{u_{ij+1} - u_{ij-1}}{2d_y} \right) \quad \text{and} \quad (\text{A2})$$

$$D_{\perp ij} = \frac{(\mathbf{d} \cdot \mathbf{n}_{\perp}) \left(\mathbf{n}_{\perp} \cdot \frac{\mathbf{v}_{ij+1} + \mathbf{v}_{i+1j} - \mathbf{v}_{i-1j} - \mathbf{v}_{ij-1}}{2} \right) + (\mathbf{e} \cdot \mathbf{n}_{\perp}) \left(\mathbf{n}_{\perp} \cdot \frac{\mathbf{v}_{ij+1} + \mathbf{v}_{i-1j} - \mathbf{v}_{i+1j} - \mathbf{v}_{ij-1}}{2} \right)}{2d_x d_y}$$

$$= \frac{n_y^2(u_{i+1j} - u_{i-1j})}{2d_x} + \frac{n_x^2(v_{ij+1} - v_{ij-1})}{2d_y} - n_x n_y \left(\frac{v_{i+1j} - v_{i-1j}}{2d_x} + \frac{u_{ij+1} - u_{ij-1}}{2d_y} \right). \quad (\text{A3})$$

These equations can be understood by replacing the boundary with the dotted lines in Fig. A1, which are meant to represent infinitesimally small line segments perpendicular to \mathbf{n} or \mathbf{n}_{\perp} ; $D_{\parallel ij}$ and $D_{\perp ij}$ represent net outflow per unit area across boundary lines perpendicular to \mathbf{n} and \mathbf{n}_{\perp} , respectively. For example, $\mathbf{d} \cdot \mathbf{n}$ in Eq. (A2) represents the total length of the dotted line segments that are perpendicular to \mathbf{n} along the side A, and $\mathbf{n} \cdot [(\mathbf{v}_{ij+1} + \mathbf{v}_{i+1j})/2]$ represents the mean flow along the side A to the direction of \mathbf{n} . Note that, as a special case of this formulation, $D_{\parallel ij} = (u_{i+1j} - u_{i-1j})/(2d_x)$ and $D_{\perp ij} = (v_{ij+1} - v_{ij-1})/(2d_y)$ when $\mathbf{n} = (\pm 1, 0)$, as expected.

REFERENCES

- Akiyama, T., 1973: Frequent occurrence of heavy rainfall along the north side to the low-level jet stream in the baiu season. *Pap. Meteor. Geophys.*, **24**, 379–388, doi:10.2467/mripapers1950.24.4_379.
- , 1990: Large, synoptic and meso scale variations of the baiu front, during July 1982. Part II: Frontal structure and disturbances. *J. Meteor. Soc. Japan*, **68**, 557–574.
- Chang, C. P., S. C. Hou, H. C. Kuo, and G. T. J. Chen, 1998: The development of an intense East Asian summer monsoon disturbance with strong vertical coupling. *Mon. Wea. Rev.*, **126**, 2692–2712, doi:10.1175/1520-0493(1998)126<2692:TDOAIE>2.0.CO;2.
- Chen, G. T. J., and C.-C. Yu, 1988: Study of low-level jet and extremely heavy rainfall over northern Taiwan in the mei-yu season. *Mon. Wea. Rev.*, **116**, 884–891, doi:10.1175/1520-0493(1988)116<0884:SOLLJA>2.0.CO;2.
- Chou, L. C., C. P. Chang, and R. T. Williams, 1990: A numerical simulation of the mei-yu front and the associated low level jet. *Mon. Wea. Rev.*, **118**, 1408–1428, doi:10.1175/1520-0493(1990)118<1408:ANSOTM>2.0.CO;2.
- Eady, E. T., 1949: Long waves and cyclone waves. *Tellus*, **1**, 33–52, doi:10.1111/j.2153-3490.1949.tb01265.x.
- Horinouchi, T., 2014: Influence of upper tropospheric disturbances on the synoptic variability of precipitation and moisture transport over summertime East Asia and the northwestern Pacific. *J. Meteor. Soc. Japan*, **92**, 519–541, doi:10.2151/jmsj.2014-602.
- Hoskins, B. J., 1982: The mathematical theory of frontogenesis. *Annu. Rev. Fluid Mech.*, **14**, 131–151, doi:10.1146/annurev.fl.14.010182.001023.
- , I. Draghici, and H. C. Davies, 1978: A new look at the ω -equation. *Quart. J. Roy. Meteor. Soc.*, **104**, 31–38, doi:10.1256/smsqj.43902.
- Huffman, G. J., and Coauthors, 2007: The TRMM Multisatellite Precipitation Analysis (TMPA): Quasi-global, multiyear, combined-sensor precipitation estimates at fine scales. *J. Hydrometeorol.*, **8**, 38–55, doi:10.1175/JHM560.1.
- Kobayashi, S., and Coauthors, 2015: The JRA-55 Reanalysis: General specifications and basic characteristics. *J. Meteor. Soc. Japan*, **93**, 5–48, doi:10.2151/jmsj.2015-001.
- Kodama, Y.-M., 1993: Large-scale common features of subtropical convergence zones (the baiu frontal zone, the SPCZ, and the SACZ). Part II: Conditions of the circulations for generating the subtropical convergence zone. *J. Meteor. Soc. Japan*, **71**, 581–610.
- Nagata, M., and Y. Ogura, 1991: A modeling case study of interaction between heavy precipitation and a low-level jet over Japan in the baiu season. *Mon. Wea. Rev.*, **119**, 1309–1336, doi:10.1175/1520-0493(1991)119<1309:AMCSOI>2.0.CO;2.
- Ninomiya, K., and T. Akiyama, 1992: Multi-scale features of baiu, the summer monsoon over Japan and East Asia. *J. Meteor. Soc. Japan*, **70**, 467–495.
- , and Y. Shibagaki, 2007: Multi-scale features of the mei-yu baiu front and associated precipitation systems. *J. Meteor. Soc. Japan*, **85B**, 103–122, doi:10.2151/jmsj.85B.103.
- Rodwell, M. J., and B. J. Hoskins, 1996: Monsoons and the dynamics of deserts. *Quart. J. Roy. Meteor. Soc.*, **122**, 1385–1404, doi:10.1002/qj.49712253408.
- Sampe, T., and S.-P. Xie, 2010: Large-scale dynamics of the mei-yu baiu rainband: Environmental forcing by the westerly jet. *J. Climate*, **23**, 113–134, doi:10.1175/2009JCLI3128.1.
- Uccellini, L. W., and D. R. Johnson, 1979: The coupling of upper and lower tropospheric jet streaks and implications for the development of severe convective storms. *Mon. Wea. Rev.*, **107**, 682–703, doi:10.1175/1520-0493(1979)107<0682:TCOUAL>2.0.CO;2.